Received: 9 August 2022 | Revised: 23 November 2022 | Accepted: 23 November 2022

DOI: 10.1111/ijac.14303

International Journal of Applied Ceramic TECHNOLOGY
Ceramic Product Development and Commercialization

RESEARCH ARTICLE

Effects of electrospraying parameters on deposition of $La_{0.3}Sr_{0.7}Fe_{0.7}Cr_{0.3}O_{3-\delta}$ cathode layer on GDC

Sedat Akkurt[1] | **Can Sındıraç**[2] | **Tuğçe Özmen Egesoy**[1] | **Gökçe Atıcı**[1] | **Elif Erişman**[1] | **Emre Erğen**[1] | **Aligül Büyükaksoy**[3]

[1] Materials Science and Engineering Department, Izmir Institute of Technology, Izmir, Turkey

[2] ASPILSAN Energy Industry and Trade Inc, Istanbul, Turkey

[3] Materials Science and Engineering Department, Gebze Technical University, Gebze, Turkey

Correspondence
S. Akkurt, Materials Science and Engineering Department, Izmir Institute of Technology, Izmir 35430, Turkey.
Email: sedatakkurt@iyte.edu.tr

Funding information
TÜBİTAK, Grant/Award Number: 121M927

Abstract

High performance in intermediate temperature solid oxide fuel cells requires improvements especially in the microstructure of the cathode layer. New cobalt-free cathode materials are used because cobalt-containing cathodes have higher thermal expansion coefficients, poor long-term chemical stability, and lower mechanical stability. Recently cobalt-free cathodes have been proposed to solve these issues by using deposition methods other than electrospray deposition (ESD). In this study, ESD method is used to develop a cobalt-free cathode layer. The electrolyte layer is gadolinium-doped ceria that is deposited with $La_{0.3}Sr_{0.7}Fe_{0.7}Cr_{0.3}O_{3-\delta}$ (LSFCr) prepared by 2-butoxyethanol and ethylene glycol solvents as opposed to conventional solvents. Experimental ESD parameters are tested at different levels and combinations by applying statistical experimental design methods to optimize the microstructure. Coating deposited as such demonstrated higher electrochemical performance than similar electrodes fabricated by other methods.

KEYWORDS
ESD, fuel cell cathode, LSFCr, SOEC, SOFC, statistical experimental design

1 | INTRODUCTION

Solid oxide fuel cells (SOFCs) are highly efficient electrochemical devices that can convert chemical energy into electricity with environmental advantages, including low emission of NO*x* and SO*x* pollutants.[1–3] Furthermore, their other superior properties (i) fuel flexibility, (ii) modularity, (iii) scaleability, (iv) silent operation, and (v) capability of operating without precious metals as catalysts make SOFCs attractive over other energy conversion devices.[4–6] There is a great interest in the development of reversible SOFCs (RSOFCs) that can be operated in two modes. The first one is the electrolysis mode (SOEC) to obtain H_2 from H_2O when excess energy is available (due to the intermittent nature of wind and solar) from renewable energy sources.[7,8] The second mode is the fuel cell (SOFC) mode that allows the use of stored hydrogen and oxygen when electricity is needed. If the cell can be operated in both the SOEC and the SOFC modes, excess energy can be generated more efficiently.[9,10]

Typical RSOFC consists of yttria-stabilized-zirconia (YSZ) electrolyte, Ni–YSZ composite as fuel electrode, and lanthanum strontium manganite (LSM)—YSZ composites as air electrodes that are quite similar to typical SOFC that needs the high temperature for operation (800–1000°C). This high-temperature operation of SOFC is costly and difficult to maintain that makes the commercialization of SOFC technology sluggish.[11] Therefore, the high operating temperature needs to be lowered to increase the expected lifetime, to reduce operating costs, to lower start-up time, and to enjoy the possibility of a wide selection of materials such as metallic interconnect materials (Fe–Cr alloy) instead of expensive ceramics materials.[2,3] Besides, this high temperature may lead to sulfur poisoning and coking at the Ni–YSZ side that dramatically compromises cell performance.[12,13] In addition to that, during the long-term operation, Ni coarsening is another major issue as it leads to diminished triple-phase boundary (TPB) length where electrode, electrolyte, and gas phases meet and the redox reactions take place.[14,15] In addition to that, LSM electrodes can be delaminated from the electrolyte layer during oxygen evolution.[14]

For all these reasons, Ni–YSZ/YSZ/LSM–YSZ materials need to be replaced with state of art materials. Using an electrolyte with higher ionic conductivity than conventional YSZ such as cerium gadolinium oxide (e.g., $Ce_{0.9}Gd_{0.1}O_{1.9}$-GDC) at intermediate operating temperature proved to be successful. Mixed ionic electronic materials (MIEC) can be operated with high durability and efficient performance in fuel and air electrodes at intermediate temperature (500–700°C).[16] To date, the most common cathode MIEC material in the past decade is $La_{1-x}Sr_xCo_{1-y}Fe_yO_{3-\delta}$ (LSCF) due to its excellent ionic and electronic conductivity and catalytic activity toward oxygen reduction.[17]

LSCF suffers from a coefficient of thermal expansion (CTE) that is significantly higher than that of the GDC electrolyte material meaning thermal stresses. Moreover, chemical stability under operating conditions is unsatisfactory due to the presence of Co(IV)/Co(III) in the structure.[18–20] To increase mechanical and chemical stability, cobalt-free MIEC materials have been extensively studied in the last decade. In addition to all the scientific limitations, cobalt also suffers from its negative socioeconomic impact during mining and processing as well as scarcity.[21–27]

Chen et al.[28] investigated $La_{0.3}Sr_{0.7}Fe_{1-y}Cr_yO_{2-d}$ for (LSFCr) for the first time in the literature. This material performed good catalytic activity during oxidation of fuels and ensured high redox stability. Moreover, the replacement of Cr instead of Co brings about a reduction in CTE from 23.0×10^{-6} to 20.9×10^{-6} K^{-1} at 700°C, respectively, that is a closer value to CTE of GDC (12.7×10^{-6} K^{-1} at 700°C). A variety of fabrication techniques have been used to prepare LSFCr for RSOFCs and approval to use that on both sides.[9,28–31] Attempts are being made to enhance the performance of SOFC and ensure stability. However, only limited production techniques are performed,[28,32–37] and there is still room for enhancement. Celikbilek et al.[38] showed that LSCF cathode layers fabricated with ESD (electro spray deposition) performed the lowest area-specific resistance (ASR) value among other methods with the same stoichiometry at intermediate temperature. However, the LSFCr electrode has not yet been fabricated via ESD. Electrospray deposition is a facile and efficient technique that does not require vacuum conditions for the production of electrode layers. Moreover, ESD allows controlling of the microstructure that helps to improve the performance of SOFC. Djurado et al.[39–46] studied the effects of electrospraying parameters on the microstructures of LSCF cathode layers. Sındıraç et al.[47] also studied the similar cathode layers but with different carrier solvents. It has been reported that cathode layers with a reticular structure can be coated on GDC electrolytes by the use of the ESD method that involves spraying a solution containing the properly formulated ionic mixtures constituting the cathode composition. ESD setup is shown in Figure 1. A high voltage maintained between the needle and the target helps create a cone jet composed of a large number of tiny droplets flying against gravity to the heated GDC electrolyte pellet that is kept above. So the flow runs against gravity and a coating can be deposited onto the GDC pellet with the desired thickness and structure. The reticular structure is desirable because of the surface area it offers for oxygen reduction reaction (ORR) and unhindered access of oxygen into TPB.

There is a great interest in development of symmetrical SOFCs (SSOFCs) that bring about increasing lifetime, reducing strains, and decreasing cost by using the same redox stable materials at the anode and cathode side.[28] Using identical anode and cathode compositions in SOFCs leads to simplifying the fabrication cost by a single step firing process via enhancement of the ease of co-sintering. These SSOFCs can be operated as RSOFCs. LSFCr that is used as the electrode material in this study is used as SSOFCs. Cathode layers in SOFC play a critical role in the electrochemical performance of the cells.

This study focuses on the improvement of the cathodic performance of symmetrical cells that is clearly controlled by the cathode microstructure developed during ESD coat-

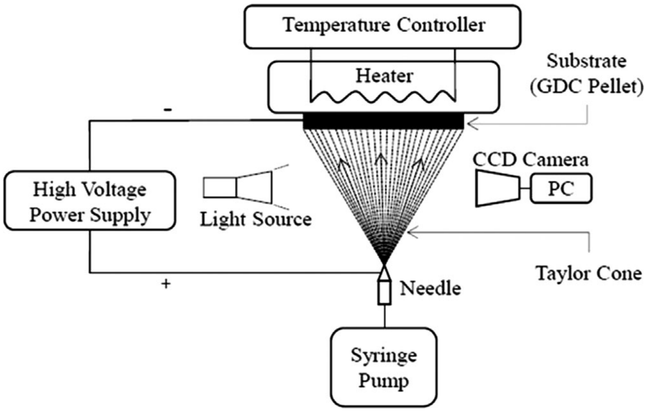

FIGURE 1 Schematic of the electrospray deposition (ESD) setup used in this study

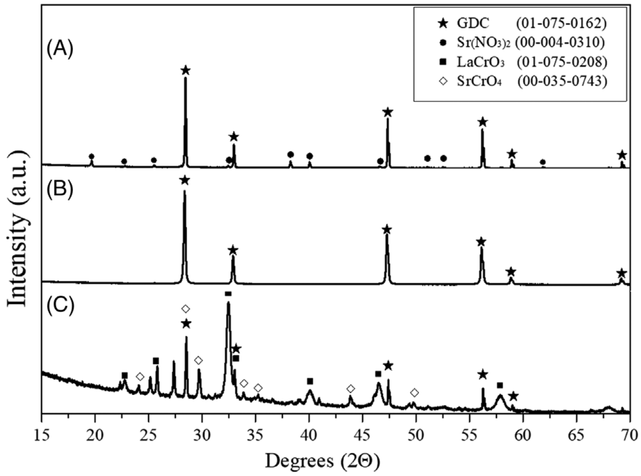

FIGURE 2 X-ray diffraction pattern for (A) LSFCr coating on gadolinium-doped ceria (GDC) pellet, (B) as-received GDC powder, and (C) LSFCr coating that is scraped off and separately heated at 700°C, 2 h. Cu K_α radiation was used in analysis.

ing. It is also well known that the latter is controlled by ESD coating parameters, such as voltage, substrate temperature, working distance (WD), flow rate, and so on. Electrochemical cell performance depends on cathode microstructure that in turn depends on ESD coating parameters. Although a thorough electrochemical characterization of the coated samples is beyond the scope of this study, some measurements are reported here.

The novelty of this manuscript lies both in the development of a cobalt-free cathode layer by ESD and in the use of design of experiments (DOE) to reduce the number of experimental runs to identify the best experimental conditions for achieving a cathode layer with desirable microstructure. The ultimate purpose is to understand how ESD factors affect the cathode layer structure.

2 | EXPERIMENTAL SETUP AND CHARACTERIZATION

Ceramic electrolyte pellets were prepared by using GDC powder (GDC, $Ce_{0.9}Gd_{0.1}O_{3-\delta}$, Fuelcellmaterials, FCM, >99%). The powder was analyzed by X-ray diffraction (XRD) as shown in Figure 2. These substrates were formed by uniaxial pressing (Carver Hydraulic Press, Wabash, IN, USA) at 180 MPa pressure into a cylindrical stainless steel die with 15 mm inner diameter. Pellet heights were about 1 mm. These compacted pellets were fired in an electrically heated laboratory kiln (Nabertherm LHT 02/17, Germany) at 1400°C for 8 h soaking time at a heating/cooling rate of 3°C/min. The densities of the pellets after firing were higher than 95% as measured by the Archimedes Method.[48]

Precursor salts solution was prepared by dissolving suitable amounts of lanthanum(III) nitrate hexahydrate (ALFA-AESAR >99.99%), strontium chloride hexahydrate (ALFA-AESAR >99%), iron(III) nitrate nonahydrate (ALFA-AESAR >99.99%), and chromium(II) nitrate nonahydrate (ALFA-AESAR >98.5%) salts in a sufficient quantity of deionized water to obtain the desired $La_{0.3}Sr_{0.7}Fe_{0.7}Cr_{0.3}O_{3-\delta}$ (LSFCr) stoichiometry. In the second step, this solution was gradually heated and stirred on a hot plate up to 80°C. Ethylene glycol ($C_2H_6O_2$, Merck >99.0%) was then slowly added into this solution until all polymerization and evaporation processes were completed. Finally, the precursor solution was diluted with ethylene glycol monobutyl ether ($C_6H_{14}O_2$, Merck >99%) (1:1 weight ratio) to reduce the surface tension and also to enhance the wetting properties of the polymeric precursor.[49–51] This last reagent was added to the solution to reach the desired final salt concentration of ions (i.e., .004 and .01 M).

ESD method was used for deposition experiments that were planned by employing Plackett–Burman screening experimental design methodology.[52]

GDC pellets that were coated with the cathode layers in the ESD setup were analyzed both for the microstructures and for the electrochemical properties as these samples were expected to function in an SOFC cell. In order to find out the ability of the ESD method, both microstructural and compositional analyses were performed by scanning electron microscopy (SEM, Philips XL-30S FEG) utilizing secondary electron imaging on cross sections of the samples. Energy-dispersive X-ray spectroscopy was used for elemental analysis. Crystal structures were examined by XRD (PANalytical X'Pert Pro). Cu K_α radiation was selected as the X-ray source. Electrochemical performances of the fabricated electrodes were evaluated by electrochemical impedance spectroscopy (EIS) analyses performed on symmetrical half-cells in the LSFCr/GDC/LSFCr configuration. For effective current collection, an in-house Ag paste was applied onto electrode surfaces. Ag wires were attached onto the Ag paste surface by applying high-temperature ceramic adhesive Ceramabond. Measurements were carried out using a BioLogic SP-150 potentiostat/galvanostat/EIS analyzer, at 500–700°C, in stagnant air. The scanned frequency range was 10^{-1}–104 Hz, whereas the excitation voltage was ±10 mV.

2.1 | Electrospray deposition (ESD)

The ESD setup used in this study is shown in Figure 1. The vertical design is made to prevent gravity-induced forces and conditions. High voltage is applied between the needle

TABLE 1 The factors and their levels selected for Plackett–Burman screening design Ref. [52]

Factor no.	Factor effects	*k*	Low level	High level
1	Flow rate	*A*	.01 ml/h	.2 ml/h
2	Voltage	*B*	7 kV	20 kV
3	Concentration	*C*	.004 M	.01 M
4	Working Distance	*D*	27 mm	50 mm
5	Temperature	*E*	300°C	350°C
6	Duration	*F*	20 min	40 min

and the electrolyte (GDC substrate). The solution that is supplied from the syringe pump feeder is sprayed upward onto the substrate from a needle tip. The GDC electrolyte substrate sits upside down on an aluminum plate with a 10 mm diameter hole. The atomized solution is deposited on the substrate by the effect of electrical field. Tip of the needle is monitored by a camera connected to a computer to observe the coating process. Coatings deposited by ESD usually appear with porous morphology owing to the nature of the process that proceeds by the flight of an ion bearing droplet of the solution onto the heated target. As the size of this droplet is very small its evaporation occurs instantly and the coating grows layer by layer. This results in a porous morphology that provides unhindered access of oxygen for ORR.

2.2 | Statistical experimental design

ESD technique involves controlling several parameters (see Table 1) that are known to affect the coating microstructure. As the number of factors to be studied is large, a thorough study (e.g., full factorial design) to cover every single combination of factor effects on coating microstructure would be cost-wise prohibitive. Although some efforts have been made in the literature[45,50] to study these effects, a statistically designed experimental approach has not yet been proposed. Hence, here we propose to employ the DOE methods[52] to minimize the number of experiments required to identify the more important factor effects.

DOE approach can help save resources by helping us avoid running a large number of experiments just to draw statistically valid conclusions.[52] Among the different possibilities like full factorial design, Box–Behnken response surface design, a Plackett–Burman screening experimental design was planned to separate the more important factor effects. The purpose was to determine that factors outweighed others. Usually screening designs are applied in the early stages of projects.[53] With this approach, a large number of experimental factors can be evaluated by the experimenter after running only a few experiments. Hence, the experimenter avoids the need to replicate experiments to reach statistically valid conclusions.[52,54] The cost of the reduction of experimental runs is the inability to identify higher order interactions among the factors.[52]

In this study, there were six continuous variables high and low levels of which are shown in Table 1. These are the ranges in which the factor effects were covered. The designed set of experiments (Plackett–Burman design) with 16 runs is shown in Table 2.

3 | RESULTS AND DISCUSSION

3.1 | Results of ESD experiments

The results obtained from the 16 experiments listed in Table 2 are shown in Table 3. The response variable showed the degree of success of the reticular structure with a maximum surface area for cathodic reaction (ORR). The variable was categorical that ranged from 1 to 5, 1 meaning poor reticular structure, and 5 meaning a well-developed reticular structure. A coating with a score of 5 is also expected to deliver a successful electrochemical performance. Examples of coating structures for each of these scores are listed in Figure 3.

In order to calculate the main factor effects, statistical calculations were done manually and are listed in Table 4 following the method described in Harris and Lautenberger's notes.[52] This procedure was also employed by Leigh et al.[54] and Kavalci et al.[55] To decide whether a factor is significant or not is determined based on the critical minimum difference (MIN) value that can be calculated by

$$S_{\mathrm{FE}} = \sqrt{1/q(\mathrm{UFE}_1^2 + \mathrm{UFE}_2^2 + \cdots + \mathrm{UFE}_q^2)} \tag{1}$$

$$[\mathrm{MIN}] = tS_{\mathrm{FE}} \tag{2}$$

where the numbers of unassigned factor effects are labeled with $q = n - p - 1$, n = number of runs ($n = 16$ for 16 run Plackett–Burman design), p is the number of factors ($p = 6$, so six factors were examined), UFE is the

TABLE 2 Experimental design layout for Plackett–Burman approach Ref. [52]

	Factor effects						**UFE (Unassigned factor effects)**								
No	***A***	***B***	***C***	***D***	***E***	***F***	***G***	***H***	***J***	***K***	***L***	***M***	***N***	***O***	***P***
1	−	−	−	+	+	+	−	+	+	+	−	−	−	+	−
2	+	−	−	−	−	+	+	+	−	−	−	−	+	+	+
3	−	+	−	−	+	−	+	+	−	+	+	−	+	−	−
4	+	+	−	+	−	−	−	+	+	−	+	−	−	−	+
5	−	−	+	+	−	−	+	+	+	−	−	+	+	−	−
6	+	−	+	−	+	−	−	+	−	+	−	+	−	−	+
7	−	+	+	−	−	+	−	+	−	−	+	+	−	+	−
8	+	+	+	+	+	+	+	+	+	+	+	+	+	+	+
9	+	+	+	−	−	−	+	−	+	+	−	−	−	+	−
10	−	+	+	+	+	−	−	−	−	−	−	−	+	+	+
11	+	−	+	+	−	+	−	−	−	+	−	−	+	−	−
12	−	−	+	−	+	+	+	−	+	−	+	−	−	−	+
13	+	+	−	−	+	+	−	−	+	−	−	+	+	−	−
14	−	+	−	+	−	+	+	−	−	+	−	+	−	−	+
15	+	−	−	+	+	−	+	−	−	−	+	+	−	+	−
16	−	−	−	−	−	−	−	−	+	+	+	+	+	+	+

TABLE 3 Experiments designed via Plackett–Burman approach Ref. [52]

Exp no	***A***	***B***	***C***	***D***	***E***	***F***	**Response (output)**
1	.01	7	.0	27	350	40	2
2	.20	7	.004	27	300	40	5
3	.01	20	.004	27	350	20	5
4	.20	20	.010	27	300	20	2
5	.01	7	.010	50	300	20	4
6	.20	7	.004	50	350	20	3
7	.01	20	.004	50	300	40	5
8	.20	20	.010	50	350	40	1
9	.20	20	.004	50	300	20	2
10	.01	20	.010	50	350	20	5
11	.20	7	.010	50	300	40	3
12	.01	7	.004	50	350	40	1
13	.20	20	.004	27	350	40	2
14	.01	20	.010	27	300	40	3
15	.20	7	.010	27	350	20	1
16	.01	7	.004	27	300	20	5[a]

[a] The best coating structure as determined by qualitative assessment.

unassigned factor effects, and $t = t_{\mathrm{dof},\alpha}$ (degrees of freedom [dof] = 9 because there were nine unassigned factor effects, $1 - \alpha$ = confidence coefficient). UFE are a mixture of two factor interactions, a list of which is available in Ref. 52.

Critical minimum differences [MIN] were computed by multiplying the different *t*-values for different confidence levels (95%, 90%, and 80%) at 9 dof with the calculated S_{FE} value. The factor effects on the response are significant if they have a greater absolute value than the calculated MIN value that is the critical limit used as a measure of significance. For example, flow rate (*A*) was significant at the 90% confidence level together with some UFE terms (see Table 4). At the 80% confidence level, flow rate (*A*) and also temperature (*E*) were significant factors. To sum up, the flow rate was evidently effective in controlling the structure of the coating. There were some interaction among some of the factors but this finding was confounded. Therefore, the next sets of experiments were planned to further investigate the effects of different flow rates on the coating structure via ladder experiments. In addition, a qualitative assessment of all coating structures revealed that sample number 16 had the best reticular structure. Hence this experiment was chosen to be the control run for the next ladder design set (A = .01, B = 7, C = .004, D = 27, E = 300, and F = 20) as shown in Figure 4.

The specimen number 16 was analyzed by XRD to identify the coating structure (Figure 2). Due to the nature of the measurement geometry, XRD signal from the electrolyte was dominant in the coated sample and peaks from the coating layer were relatively overshadowed (Figure 2A). However, $SrNO_3$ salt was still detected in the coating layer. Because the spray coating process was done at 300°C, this salt was expected.[56] Hence the coating was scraped off from the electrolyte surface and heated at

TABLE 4 Evaluation of the Plackett–Burman Design

Run order	*A* Flow rate	*B* Voltage	*C* Concentration	*D* Working distance	*E* Temperature	*F* Duration	*G*	*H*	*J*	*K*	*L*	*M*	*N*	*O*	*P*
1	−	−	−	+	+	+	−	+	+	+	−	−	−	+	−
2	+	−	−	−	−	+	+	+	−	−	−	−	+	+	+
3	−	+	−	−	+	−	+	+	−	+	+	−	+	−	−
4	+	+	−	+	−	−	−	+	+	−	+	−	−	−	+
5	−	−	+	+	−	−	+	+	+	−	−	+	+	−	−
6	+	−	+	−	+	−	−	+	−	+	−	+	−	−	+
7	−	+	+	−	−	+	−	+	−	−	+	+	−	+	−
8	+	+	+	+	+	+	+	+	+	+	+	+	+	+	+
9	+	+	+	−	−	−	+	−	+	+	−	−	−	+	−
10	−	+	+	+	+	−	−	−	−	−	−	−	+	+	+
11	+	−	+	+	−	+	−	−	−	+	−	−	+	−	−
12	−	−	+	−	+	+	+	−	+	−	+	−	−	−	+
13	+	+	−	−	+	+	−	−	+	−	−	+	+	−	−
14	−	+	−	+	−	+	+	−	−	+	−	+	−	−	+
15	+	−	−	+	+	−	+	−	−	−	+	+	−	+	−
16	−	−	−	−	−	−	−	−	+	+	+	+	+	+	+
Sum +	19	25	24	21	20	22	22	27	19	24	23	24	30	26	25
Sum −	−30	−24	−25	−28	−29	−27	−27	−22	−30	−25	−26	−25	−19	−23	−24
Over-all Sum	49	49	49	49	49	49	49	49	49	49	49	49	49	49	49
Difference	−11	1	−1	−7	−9	−5	−5	5	−11	−1	−3	−1	11	3	1
Effect	−1.375	.125	−.125	−.875	−1.125	−.625	−.625	.625	−1.375	−.125	−.375	−.125	1.375	.375	.125
					S_{FE}=	.737									
t distribution	$t_{9,0.1}$	1.38			MIN=	1.017		%80 Confidence level							
	$t_{9,0.05}$	1.83			MIN=	1.351		%90 Confidence level							
	$t_{9,0.025}$	2.26			MIN=	1.666		%95 Confidence level							

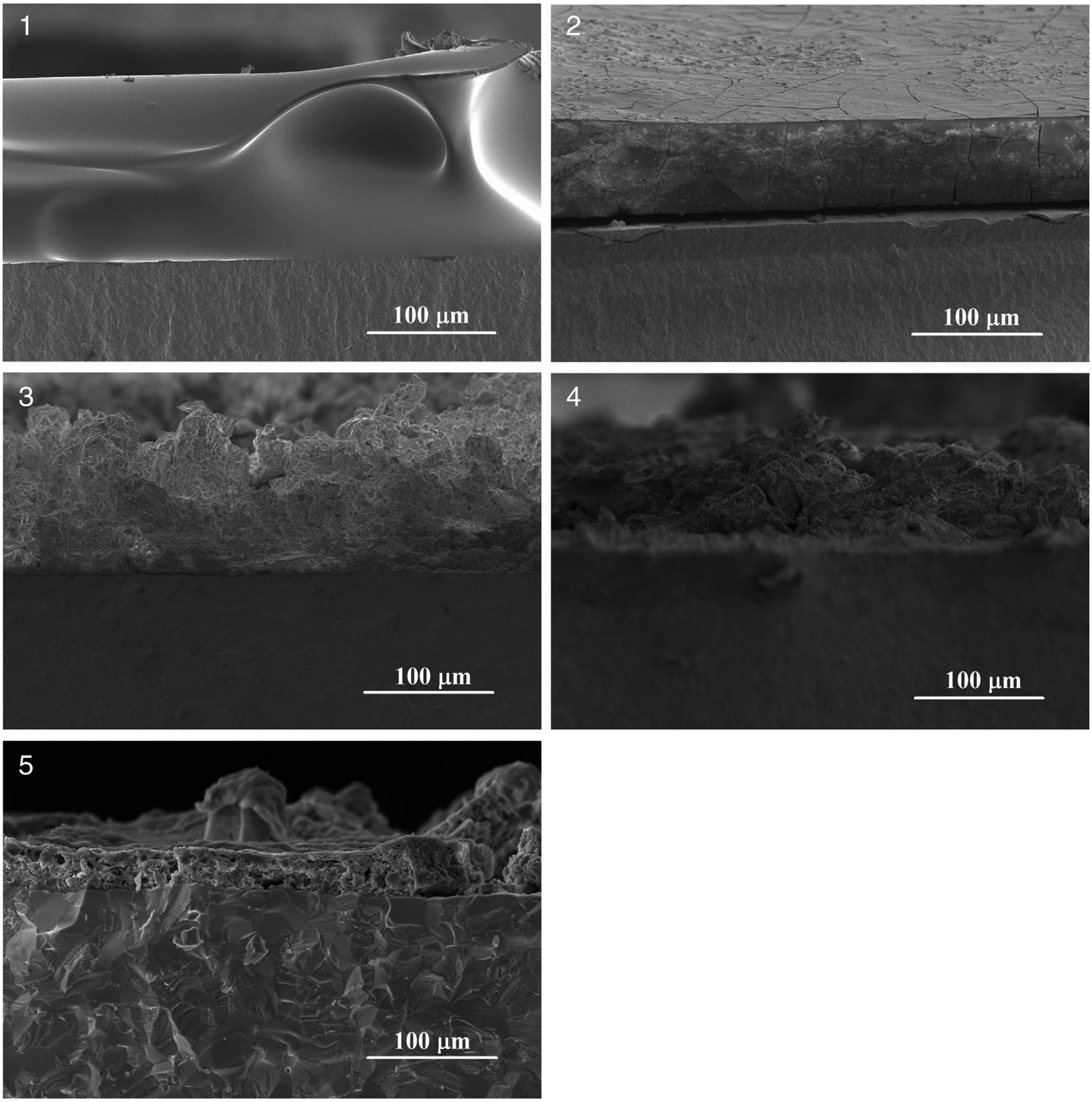

FIGURE 3 Grading of the reticular structures (1–5) for the response variable. Top left figure represents a dense and glassy coating with a score of 1, top right figure has more porosity with a score of 2, middle row left figure shows a relatively more porous structure with a score of 3, middle row right figure has further higher reticular structure with a score of 4 and the bottom third row figure has the best reticular structure with a score of 5

700°C for 2 h in an electric kiln to mimic operation conditions and to avoid strong signals from the GDC layer. New mixed oxides like $LaCrO_3$ and $SrCrO_4$ were found to have formed in the coating layer (Figure 2C). Considering the long operation times of the SOFC cell at temperatures around 700°C, these new mixed oxides are expected to eventually form.

3.2 | The effect of the flow rate

Having successfully identified the best coating test condition to be the sample 16, we performed three more experiments by varying the flow rate as listed in Figure 4 where the effect of elevating the flow rate on increasing coating thickness can be clearly seen.

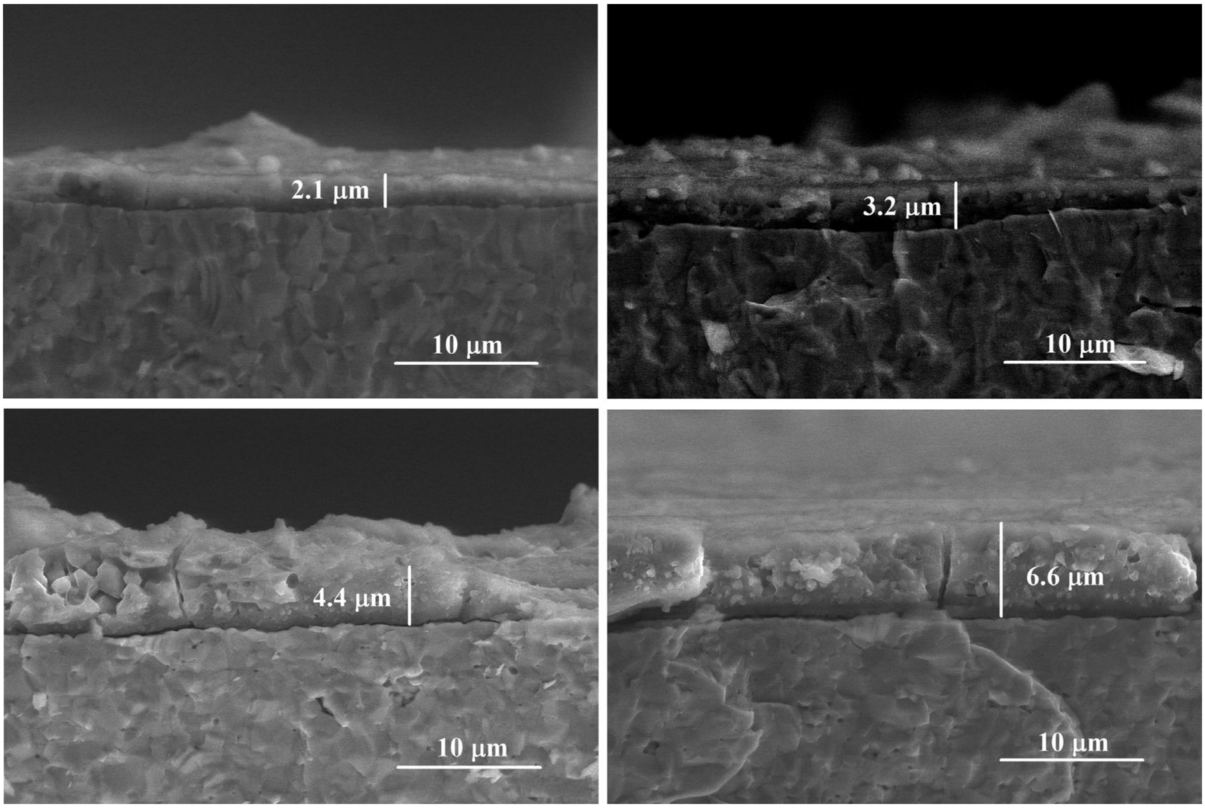

FIGURE 4 Ladder design experiments to investigate the effect of flow rate on the coating structure.Top row left (.005ml/h), top row right (.010ml/h), bottom row left (.015ml/h), bottom row right (.020ml/h)

3.3 | Microstructural analyses (SEM)

It is known that the deposition parameters affect the resulting coating microstructures as listed in Table 3. Samples coded 3 and 16 provided the best reticular structures with coating thicknesses between 2 and 3 μm (Figure 5A,B). Sample 16 was further analyzed by SEM–EDS to check and verify the resulting compositions to yield correct stoichiometry as shown in Figure 6.

The coating is deposited in three stages: flight of a small droplet, its impact on the GDC surface and evaporation of volatile constituents with the eventual formation of mixed ion oxide in a reticulated form due to the violent fluid flow.[45] The distance between the tip of the needle and the substrate is called the WD. If WD is small or voltage is high then there is little time for solvent evaporation and hence larger droplets form. The substrate temperature was kept higher than the boiling point of the precursor solution, which may have contributed to changes in initial droplet size during coating.[45] Increasing the temperature leads to accelerated evaporation rate which ends up forming smaller droplets. All parameters are probably related to each other, and a highly porous microstructure is formed with large surface area as observed in cross-sectional views of the deposited electrolyte in SEM (Figure 5). Increasing the reticular structure can offer more surface area for ORR.

As the reticular structure is desirable, all samples listed in Table 3 were observed in SEM to be graded for the degree of reticular structure formation. But not all of these SEM images are given here for the sake of brevity. XRD analysis of sample 16 revealed the presence of strong peaks for GDC as well as smaller peaks for $Sr(NO_3)_2$. The latter was a surprise as the precursor solution was prepared by dissolving $SrCl_2$, not $Sr(NO_3)_2$.[57]

3.4 | Electrochemical impedance spectroscopy (EIS)

Symmetrical half-cells were constructed in the electrode/GDC electrolyte/electrode configuration for electrochemical performance analysis. Sample 16 was employed as symmetrical half-cell electrodes, simply due to its optimized fabrication conditions. Figure 7A provides the impedance response of the symmetrical half-cells with sample 16 electrodes in the form of Nyquist (main graph) and Bode (inset) plots. An equivalent circuit consisting of two resistors, each connected in parallel to a constant phase element (ASR2CPE2 and ASR3CPE3) and a

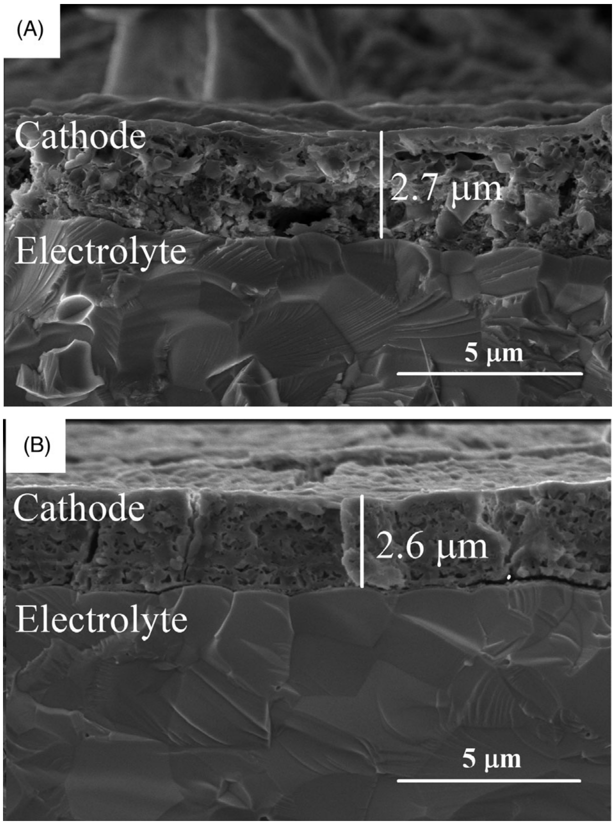

FIGURE 5 Scanning electron microscopy (SEM) images of the cross sectional views of a $La_{0.3}Sr_{0.7}Fe_{0.7}Cr_{0.3}O_{3-\delta}$ (LSFCr) coating deposited on gadolinium-doped ceria (GDC) electrolyte. Samples 3 and 16 were coated by using applied voltage and substrate temperatures of (A) 20 kV and 350°C, (B) 7 kV and 300°C, respectively. X-ray diffraction (XRD) pattern for the specimen shown in (B) is available in Figure 2.

serial resistor (ASR1) was used to fit the impedance data. Here, ASR1 referred to resistance to oxygen transport through the GDC electrolyte and any additional current collection resistances, whereas ASR2 and ASR3 referred to resistances associated with electrochemical processes that occurred at high and low frequencies, respectively. The sum of ASR2 and ASR3 (ASR_{total}) corresponded to the polarization resistances of the two electrodes of the symmetrical half-cell, which meant that, to determine the polarization resistance of a single electrode ($ASR_{electrode}$), ASR_{total} had to be divided by two.

Table 5 shows the results of the equivalent circuit fittings performed on impedance data collected at 550–700°C. At 700°C, an $ASR_{electrode}$ value of .26 Ω cm^2 was obtained. In the literature, Molero-Sanchez et al. fabricated $La_{0.3}Ca_{0.7}Fe_{0.7}Cr_{0.3}O_{3-\delta}$ (LCFCr) electrodes by depositing a paste containing the combustion-derived powders onto GDC electrolytes and sintering them at 1000°C.[46] The electrode yielded an $ASR_{electrode}$ value of .73 Ω cm^2 at 700°C, which roughly corresponds to

TABLE 5 Summary of area-specific resistance, capacitance, and summit frequency values extracted from the equivalent circuit fittings via $C = (ASR \times p)^{(1/n)}/ASR$ where, p and n are fit parameters

Temperature (°C)	ASR1 (Ω cm^2)	ASR2 (Ω cm^2)	ASR3 (Ω cm^2)	*p2*	*n2*	*C2* (F/cm^2)	*f2* (Hz)	*p3*	*n3*	*C3*(F/cm^2)	*f3* (Hz)
700	3.21	.2	.314	.00417	.81	7.79E-04	1020	.00889	.88	4.06E-03	125
650	4.671	.319	.797	.00238	.85	6.71E-04	744	.0066	.8	3.40E-03	59
600	7.15	.45	2.45	.0013	.9	5.69E-04	622	.008	.8	3.00E-03	22
550	11.7	.74	7.7	.0012	.83	2.85E-04	756	.0056	.77	2.19E-03	9

Note: Summit frequency values were calculated via $f = 1/(2\pi \times ASR \times C)$. Errors associated with the ASR, p, and n parameters determined through the equivalent circuit fittings were below 15%.

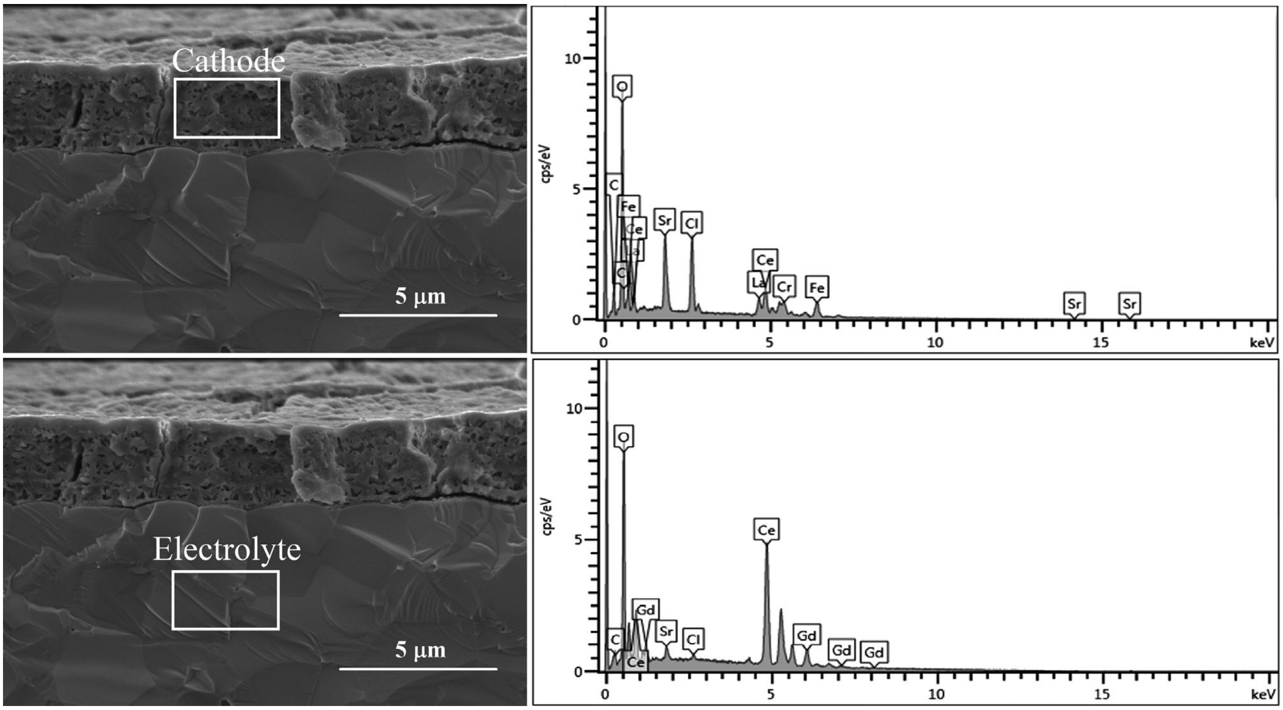

FIGURE 6 Elemental compositions of electro-sprayed gadolinium-doped ceria (GDC) pellet sample coded #16: (A) cathode layer and (B) electrolyte layer as analyzed by EDS

three times the $\text{ASR}_{\text{electrode}}$ value obtained here from ESD-derived LSFCr electrodes. In another study, Molero-Sanchez et al. fabricated LCFCr electrodes by a microwave-based methods, which yielded an $\text{ASR}_{\text{electrode}}$ value of .25 Ω cm^2, but at 800°C.[58] Utilizing the optimized ESD method to fabricate a comparable LSFCr electrode evidently reduced the operating temperature by 100°C, without any loss in electrochemical performance.

In order to understand what electrochemical processes ASR2 and ASR3 correspond to and determine what the rate limiting mechanisms of the overall ORR over the ESD-derived LSFCr electrodes are (i) summit frequencies of the ASR-CPE couples and (ii) temperature dependencies of (i.e., activation energies) of the respective resistances (Figure 7) were examined. The high-frequency process, defined by ASR2-CPE2 was associated with capacitances around 10^{-4} F/cm^2 over the temperature range of 550–700°C (Table 5). These low capacitances, along with the relatively high "*n*" values that are indicative of semicircular shapes[59,60] suggest that the high-frequency process is oxygen transfer at the LSFCr electrode/GDC electrolyte interface. The rate of oxygen transfer at the electrode/electrolyte interface should be determined by the oxygen ion conductivity of GDC. Therefore, the similar activation energies of ASR1 (oxygen transport through the GDC electrolyte) and of ASR2 (Figure 7B) further supports our hypothesis that ASR2 indicated the rate of oxygen transfer at the electrode/electrolyte interface.

ASR3 is associated with capacitances of ca. 10^{-3} F/cm^2 in the 550–700°C temperature range (Table 5) and a relatively high activation energy of 1.50 eV (Figure 7B). In other MIEC electrodes that have been studied more frequently than LCFCr, such as; (La, Sr)CoO_3 and (La, Sr) (Co, Fe)O_3 films, the reported capacitance values associated with the low-frequency rate-limiting step varied depending on the microstructure.[19,41,61–67] For example, MIEC electrodes that had dense microstructures were reported to exhibit a low-frequency rate limiting processes with associated capacitances of 10^{-2}–10° F/cm^2.[19,41,61–63] On the other hand, EIS measurements performed on porous MIEC cathodes yielded rate limiting low-frequency responses with capacitances of 10^{-4}–10^{-3} F/cm^2, which is in the range of what has been observed in the present case.[63–67] Regardless the capacitance value, all the rate limiting low-frequency values were ascribed to oxygen exchange at the electrode surface.[19,41,61–67]

A possible explanation to the apparent discrepancy is related to the extent of lattice involvement, induced by differences in microstructure. For example, porous electrodes have surfaces available for oxygen adsorption that are distributed throughout the electrode, and thus, oxygen adsorption can take place over large surface areas, some of which are close to the electrolyte. In this case, adsorbed oxygen may be transported to the electrolyte via the surface of the electrode as well as its bulk. On the other hand, in the case of dense electrodes, oxygen adsorption is mainly

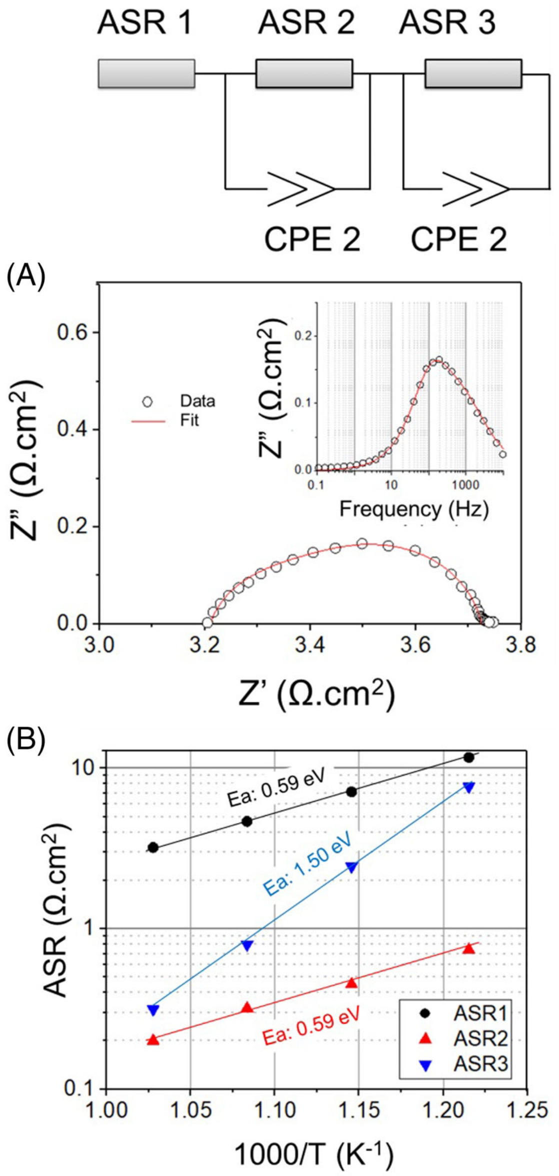

FIGURE 7 (A) Impedance response of the symmetrical half-cells with sample 16 electrodes, collected at 700°C, in stagnant air. Equivalent circuit used to fit the impedance data is also provided above the Nyquist and Bode plots. (B) Temperature dependence of the area-specific resistance components of the overall impedance response, namely, ASR1, ASR 2, and ASR 3, respectively

limited to the top surface of the electrode, forcing the take the bulk path to reach the electrolyte. Consequently, oxygen reduction involves the lattice to a greater extent in dense MIEC electrodes, compared to porous ones, yielding a larger chemical capacitance in dense electrodes.[68,69] The relatively low capacitances of ca. 10^{-3} F/cm^2 obtained in the rate limiting low-frequency process detected by the EIS measurements of the ESD-derived LCFCr cathodes, in the present case, is therefore likely caused by the large surface area enabled by the porous microstructure (Figure 6).

Another aspect of the surface oxygen adsorption-related chemical capacitance is that its magnitude depends on the amount of B-site transition metal cations that may be oxidized in response to the oxygen ion replacement by the oxygen vacancy.[17] This, in turn, corresponds to a dependence of the capacitance on the total volume of the electrode. In this context, the lower frequency capacitance value obtained in the present case of ESD-derived porous LSFCr in comparison to porous LCFCr fabricated by sintering screen-printed powders is connected to the difference in thicknesses. The thinner coatings obtained here (thickness of ca. 6 μm) contain smaller amounts of transition metal cations to be oxidized upon oxygen adsorption onto the electrode surface in comparison to those present in the 25 μm-thick electrode in the work by Molero-Sanchez et al.,[70] yielding smaller capacitances.

4 | CONCLUSION

LSFCr cathode layers were successfully coated on GDC electrolyte by ESD method. Statistical experimental design methodology was employed to plan the experimental conditions in the search for optimal coating microstructure. Plackett–Burman design method helped minimize the number of experimental runs necessary to identify the best conditions for the ideal coating microstucture. The best reticular structure was possible with sample 16 that was coated using a flow rate of .01 ml/h, a voltage of 7 kV, a concentration of .004 M, a WD of 27 mm, a temperature of 300°C, and a coating duration of 20 min. The coating stoichiometry was confirmed to have the correct composition of the LSFCr (3773). Ladder design experiments were also performed to investigate the effect of flow rate on coating thickness and quality. EIS measurements showed favorable ASR values of .22 Ω cm^2 at 700°C.

ACKNOWLEDGMENT

The work reported here has been supported by TÜBİTAK through Project No: 121M927.

ORCID

Sedat Akkurt https://orcid.org/0000-0002-2534-5756
Can Sındıraç https://orcid.org/0000-0002-9935-1331

REFERENCES

1. Stambouli AB, Traversa E. Solid oxide fuel cells (SOFCs): a review of an environmentally clean and efficient source of energy. Renew Sustain Energy Rev. 2002;6(5):433–55. https://doi.org/10.1016/S1364-0321(02)00014-X
2. Mahato N, Banerjee A, Gupta A, Omar S, Balani K. Progress in material selection for solid oxide fuel cell technology: a review. Prog Mater Sci. 2015;72:141–337. https://doi.org/10.1016/j.pmatsci.2015.01.001

3. Ramadhani F, Hussain MA, Mokhlis H, Hajimolana S. Optimization strategies for solid oxide fuel cell (SOFC) application: a literature survey. Renew Sustain Energy Rev. 2017;76:460–84. https://doi.org/10.1016/j.rser.2017.03.052
4. Sındıraç C, Akkurt S. Formation of La1−xSrxCo1−yFeyO3−δ cathode materials from precursor salts by heating in contact with CGO electrolyte. Int J Hydrogen Energy. 2016;41(40):18157–65. https://doi.org/10.1016/j.ijhydene.2016.07.143
5. Xu Q, Guo Z, Xia L, He Q, Li Z, Bello IT, et al. A comprehensive review of solid oxide fuel cells operating on various promising alternative fuels. Energy Convers Manage. 2022;253:115175. https://doi.org/10.1016/j.enconman.2021.115175
6. Abdalla AM, Hossain S, Azad AT, Petra PM, Begum F, Eriksson SG, et al. Nanomaterials for solid oxide fuel cells: a review. Renew Sustain Energy Rev. 2018;82(Part 1):353–68. https://doi.org/10.1016/j.rser.2017.09.046
7. Kim S, Joh DW, Lee DY, Lee J, Kim HS, Khan MZ, et al. Microstructure tailoring of solid oxide electrolysis cell air electrode to boost performance and long-term durability. Chem Eng J. 2021;410:128318. https://doi.org/10.1016/j.cej.2020.128318
8. Laguna-Bercero MA. Recent advances in high temperature electrolysis using solid oxide fuel cells: a review. J Power Sources. 2012;203:4–16. https://doi.org/10.1016/j.jpowsour.2011.12.019
9. Addo PK, Molero-Sanchez B, Chen M, Paulson S, Birss V. CO/CO_2 study of high performance $La_{0.3}Sr_{0.7}Fe_{0.7}Cr_{0.3}O_{3-\delta}$ reversible SOFC electrodes. Fuel Cells. 2015;15(5):689–96.
10. Mogensen MB, Chen M, Frandsen HL, Graves C, Hansen JB, Hansen KV, et al. Reversible solid-oxide cells for clean and sustainable energy. Clean Energy. 2019;3(3):175–201. https://doi.org/10.1093/ce/zkz023
11. Molero-Sánchez B, Addo P, Buyukaksoy A, Birss V. GDC-infiltrated La0.3Ca0.7Fe0.7Cr0.3O3-δ symmetrical oxygen electrodes for reversible SOFCs. ECS Trans. 2015;66:185. https://doi.org/10.1149/06602.0185ecst
12. Addo P, Molero-Sánchez B, Buyukaksoy A, Birss V. Sulfur tolerance of La0.3M0.7Fe0.7Cr0.3O3-δ (M = Sr, Ca) solid oxide fuel cell anodes. ECS Trans. 2015;66:219. https://doi.org/10.1149/06602.0219ecst
13. Cheng Z, Zha S, Liu M. Influence of cell voltage and current on sulfur poisoning behavior of solid oxide fuel cells. J Power Sources. 2007;172(2):688–93. https://doi.org/10.1016/j.jpowsour.2007.07.052
14. Buyukaksoy A, Petrovsky V, Dogan F. Redox stability of Ni-YSZ cermets prepared by polymeric precursor infiltration. ECS Trans. 2012;45:509. https://doi.org/10.1149/1.3701342
15. Buyukaksoy A, Petrovsky V, Dogan F. Optimization of redox stable Ni-YSZ anodes for SOFCs by two-step infiltration. J Electrochem Soc. 2012;159:F841. https://doi.org/10.1149/2.075212jes
16. Buyukaksoy A, Petrovsky V, Dogan F. Stability and performance of solid oxide fuel cells with nanocomposite electrodes. J Electrochem Soc. 2012;159:B666. https://doi.org/10.1149/2.050206jes
17. Adler SB. Factors governing oxygen reduction in solid oxide fuel cell cathodes†. Chem Rev. 2004;104(10):4791–844. https://doi.org/10.1021/cr020724o
18. Tai LW, Nasrallah MM, Anderson HU, Sparlin DM, Sehlin SR. Structure and electrical properties of La1−xSrxCo1−yFeyO3. Part 1. The system La0.8Sr0.2Co1−yFeyO3. Solid State Ionics. 1995;76:259–71.
19. Tai LW, Nasrallah MM, Anderson HU, Sparlin DM, Sehlin SR. Structure and electrical properties of La1−xSrxCo1− yFeyO3. Part 2. The system La1−xSrxCo0.2Fe0.8O3. Solid State Ionics. 1995;76:273–83.
20. Xiao J, Xu Q, Huang DP, Chen M, Zhao K, Kim BK. Evaluation of La0.3Ca0.7Fe1−yCryO3−δ (y = 0.1–0.3) cathodes for intermediate temperature solid oxide fuel cells. Mater Res Bull. 2017;90:104–10.
21. Bamana G, Miller JD, Young SL, Dunn JB. Addressing the social life cycle inventory analysis data gap: insights from a case study of cobalt mining in the Democratic Republic of the Congo. One Earth. 2021;4(12):1704–14.
22. Wilburn DR. Cobalt mineral exploration and supply from 1995 through 2013. US Department of the Interior, US Geological Survey Scientific Investigations Report. 2012;2011–5084.
23. Shedd KB, McCullough EA, Bleiwas DI. Global trends affecting the supply security of cobalt. Min Eng. 2017;69(12):37–42.
24. Muralidharan N, Self EC, Nanda J, Belharouak I. Next-generation cobalt-free cathodes–a prospective solution to the battery industry's cobalt problem. Adv Energy Mater. 2022;12:33–53.
25. Muralidharan N, Self EC, Nanda J, Belharouak I. Next-Generation Cobalt-Free Cathodes–A Prospective Solution to the Battery Industry's Cobalt Problem. Transition Metal Oxides for Electrochemical Energy Storage, in Advanced Energy Materials. 2022;12(9). https://doi.org/10.1002/aenm.202103050
26. Banza Lubaba Nkulu C, Casas L, Haufroid V, De Putter T, Saenen ND, Kayembe-Kitenge T, et al. Sustainability of artisanal mining of cobalt in DR Congo. Nature Sustainability. 2018;1(9):495–504.
27. Tsurukawa N, Prakash S, Manhart A. Social impacts of artisanal cobalt mining in Katanga, Democratic Republic of Congo. Freiburg: Öko-Institut eV; 2011.
28. Chen M, Paulson S, Thangadurai V, Birss V. Sr-rich chromium ferrites as symmetrical solid oxide fuel cell electrodes. J Power Sources. 2013;236:68–79.
29. Ruiz-Morales JC, Marrero-López D, Canales-Vázquez J, Irvine JTS. Symmetric and reversible solid oxide fuel cells. RSC Adv. 2011;1(8):1403–14. https://doi.org/10.1039/c1ra00284h
30. Bastidas DM, Tao S, Irvine JTS. A symmetrical solid oxide fuel cell demonstrating redox stable perovskite electrodes. J Mater Chem. 2006;16(17):1603–5. https://doi.org/10.1039/b600532b
31. Zhou Q, Yuan C, Han D, Luo T, Li J, Zhan Z. Evaluation of $LaSr_2Fe_2CrO_{9-\delta}$ as a potential electrode for symmetrical solid oxide fuel cells. Electrochim Acta. 2014;133:453–8.
32. Addo P, Molero-Sanchez B, Buyukaksoy A, Paulson S, Birss V. Sulfur tolerance of La0.3M0.7Fe0.7Cr0.3O3-δ (M = Sr, Ca) solid oxide fuel cell anodes. ECS Trans. 2015;66(2):219–28.
33. Addo PK, Molero-Sanchez B, Chen M, Paulson S, Birss V. CO/CO_2 study of high performance $La_{0.3}Sr_{0.7}Fe_{0.7}Cr_{0.3}O_{3-\delta}$ reversible SOFC electrodes. Fuel Cells. 2015;15(5):689–96.
34. Addo P, Mulmi S, Molero-Sánchez B, Keyvanfar P, Thangadurai V, Birss V. In: Performance Enhancement of La0. 3Sr0. 7Fe0. 7Cr0. 3O3 (LSFCr) Electrodes in CO2/CO Atmosphere. ECS Meeting Abstracts (No. 40). IOP Publishing; 2016. p. 3041.
35. Chen M, Chen D, Chang M, Hu H, Xu Q. New Insight into hydrogen oxidation reaction on $La_{0.3}Sr_{0.7}Fe_{0.7}Cr_{0.3}O_{3-\delta}$ perovskite as a solid oxide fuel cell anode. J Electrochem Soc. 2017;164:F405–11. https://doi.org/10.1149/2.1571704jes

36. Kozokaro VF, Addo PK, Ansari HM, Birss VI, Toroker MC. Optimal oxygen vacancy concentration for CO_2 reduction in LSFCr perovskite: a combined density functional theory and thermogravimetric analysis measurement study. J Phys Chem C. 2020;124(50):27453–66.
37. Molero-Sanchez B, Addo P, Buyukaksoy A, Paulson S, Birss V. Faraday Discuss. 2015;182:159–75.
38. Celikbilek Ö, Jauffrès D, Siebert E, Dessemond L, Burriel M, Martin CL, et al. Rational design of hierarchically nanostructured electrodes for solid oxide fuel cells. J Power Sources. 2016;333:72–82.
39. Marinha D, Dessemond L, Scott Cronin J, Wilson JR, Barnett SA, Djurado E. Microstructural 3D reconstruction and performance evaluation of LSCF cathodes obtained by electrostatic spray deposition. Chem Mater. 2011;23,24:5340–8. https://doi.org/10.1021/cm2016998
40. Çelikbilek Ö, Siebert E, Jauffrès D, Martin CL, Djurado E. Influence of sintering temperature on morphology and electrochemical performance of LSCF/GDC composite films as efficient cathode for SOFC. Electrochim Acta. 2017;246:1248–58. https://doi.org/10.1016/j.electacta.2017.06.070
41. Marinha D, Dessemond L, Djurado E. Electrochemical investigation of oxygen reduction reaction on $La_{0.6}Sr_{0.4}Co_{0.2}Fe_{0.8}O_{3-\delta}$ cathodes deposited by electrostatic spray deposition. J Power Sources. 2012;197:80–7. https://doi.org/10.1016/j.jpowsour.2011.09.049
42. Marinha D, Hayd J, Dessemond L, Ivers-Tiffée E, Djurado E. Performance of $(La,Sr)(Co,Fe)O_{3-x}$ double-layer cathode films for intermediate temperature solid oxide fuel cell. J Power Sources. 2011;196(11):5084–90. https://doi.org/10.1016/j.jpowsour.2011.01.063
43. Marinha D, Rossignol C, Djurado E. Influence of electrospraying parameters on the microstructure of $La_{0.6}Sr_{0.4}Co_{0.2}F_{0.8}O_{3-a}$0.6Sr0.4Co0SOFCs. J Solid State Chem. 2009;182(7):1742–8. https://doi.org/10.1016/j.jssc.2009.04.018
44. Sar J, Charlot F, Almeida A, Dessemond L, Djurado E. Coral Microstructure of Graded CGO/LSCF Oxygen Electrode by Electrostatic Spray Deposition for Energy (IT-SOFC, SOEC), Chapter 3 in Special Issue: Fundamentals & Developments of Fuel Cells Conference 2013 (FDFC2013) June. 2014. p. 357–63. https://doi.org/10.1002/fuce.201300146
45. Marinha D, Dessemond L, Djurado E. Microstructure-electrical properties of original LSCF films deposited by ESD for IT-SOFCs. ECS Trans. 2019;28(11):93–103. https://doi.org/10.1149/1.3495835
46. Marinha D, Dessemond L, Djurado E. Comparison of electrochemical performances of electrosprayed LSCF cathode films for IT-SOFCS for different morphologies and cobalt contents. ECS Trans. 2011;35(1):2283.
47. Sındıraç C, Akkurt S. Microstructural investigation of the effect of electrospraying parameters on LSCF films. Int J Hydrogen Energy. 2020;45(60):35139–48. https://doi.org/10.1016/j.ijhydene.2020.02.194
48. Astm C20. Standard Test Methods for Apparent Porosity, Water Absorption, Apparent Specific Gravity, and Bulk Density of Burned Refractory Brick and Shapes by Boiling Water 1 This international standard was developed in accordance with internationally recognized pri. vol. 00. ASTM Int; 2015. p. 20–2. 2017. https://doi.org/10.1520/C0020-00R10
49. Sındıraç C, Çakırlar S, Büyükaksoy A, Akkurt S. Lowering the sintering temperature of solid oxide fuel cell electrolytes by infiltration. J Eur Ceram Soc. 2019;39(2–3):409–17. https://doi.org/10.1016/j.jeurceramsoc.2018.09.029
50. Sındıraç C, Büyükaksoy A, Akkurt S. Electrical properties of gadolinia doped ceria electrolytes fabricated by infiltration aided sintering. Solid State Ionics. 2019;340:115020. https://doi.org/10.1016/j.ssi.2019.115020
51. Sındıraç C, Ahsen A, Ozturk O, Akkurt S, Birss VI, Buyukaksoy A. Fabrication of LSCF and LSCF-GDC nanocomposite thin films using polymeric precursors. Ionics (Kiel). 2020;26(2):913–25. https://doi.org/10.1007/s11581-019-03262-4
52. Harris H, Lautenberger W. Strategy of experimentation, E.I. Dupont de Nemours & Co. Inc. Short Course Notes; Wilmington, Del., USA, 1976.
53. D.C. Montgomery. Design and analysis of experiments. 6th ed. USA: John Wiley & Sons Inc.; 2005.
54. Leigh HD, Towe CA. Use of a screening experimental design to develop a high Al2O3 casting slip. Am Ceram. Soc. Bull. 1987;66(5):786–9.
55. Kavalci S, Yalamaç E, Akkurt S. Effects of boron addition and intensive grinding on synthesis of anorthite ceramics. Ceram Int. 2008;34(7):1629–35. https://doi.org/10.1016/j.ceramint.2007.07.007
56. Sındıraç C, Akkurt S. Formation of La1-xSrxCo1-yFeyO3-d cathode materials from precursor salts by heating in contact with CGO electrolyte. Int J Hydrogen Energy. 2016;41(18157):e18165.
57. Sındıraç C. Investigation of The Formation of La1-xSrxCo1-yFeyO3-d Cathode Materials And Their Interaction with Electrolyte Substrates for Potential IT-SOFC Applications, Master's Thesis (No:342933), Izmir Institute of Technology. Izmir, Turkey, 2013.
58. Molero-Sanchez B, Moran E, Birss V. Rapid and low-energy fabrication of symmetrical solid oxide cells by microwave methods. ACS Omega. 2017;2:3716–23.
59. Hansen KK. Evaluation of LSF based SOFC cathodes using cone-shaped electrodes and EIS. Solid State Ionics. 2020;344:115096.
60. Baumann FS, Fleig J, Habermeier H-U, Maier J. Impedance spectroscopic study on well-defined (La,Sr)(Co,Fe)O3−δ model electrodes. Solid State Ionics. 2006;177(11):1071–81.
61. Rupp GM, Téllez H, Druce J, Limbeck A, Ishihara T, Kilner J, et al. Surface chemistry of La 0.6 Sr 0.4 CoO 3− δ thin films and its impact on the oxygen surface exchange resistance. J Mater Chem A. 2015;3(45):22759–69.
62. Peters C, Weber A, Ivers-Tiffée E. Nanoscaled (La0. 5Sr0. 5) CoO3− δ thin film cathodes for SOFC application at 500°C< T< 700°C. J Electrochem Soc. 2008;155(7):B730.
63. Karageorgakis NI, Heel A, Bieberle-Hütter A, Rupp JL, Graule T, Gauckler LJ. Flame spray deposition of La0. 6Sr0. 4CoO3− δ thin films: microstructural characterization, electrochemical performance and degradation. J Power Sources. 2010;195(24):8152–61.
64. Adler SB. Mechanism and kinetics of oxygen reduction on porous La1− xSrxCoO3− δ electrodes. Solid State Ionics. 1998;111(1–2):125–34.
65. Adler SB, Lane JA, Steele BCH. Electrode kinetics of porous mixed-conducting oxygen electrodes. J Electrochem Soc. 1996;143(11):3554.

66. Januschewsky J, Ahrens M, Opitz A, Kubel F, Fleig J. Optimized La0. 6Sr0. 4CoO3–δ thin-film electrodes with extremely fast oxygen-reduction kinetics. Adv Funct Mater. 2009;19(19):3151–6.
67. Baumann FS, Fleig J, Habermeier HU, Maier J. Impedance spectroscopic study on well-defined (La, Sr)(Co, Fe) O3− δ model electrodes. Solid State Ionics. 2006;177(11–12):1071–81.
68. Simrick NJ, Bieberle-Hütter A, Ryll TM, Kilner JA, Atkinson A, Rupp JLM. An investigation of the oxygen reduction reaction mechanism of La0. 6Sr0. 4Co0. 2Fe0. 8O3 using patterned thin films. Solid State Ionics. 2012;206:7–16.
69. Yang YL, Chen CL, Chen SY, Chu CW, Jacobson AJ. Impedance studies of oxygen exchange on dense thin film electrodes of La0. 5Sr0. 5CoO3− δ. J Electrochem Soc. 2000;147(11):4001.
70. Molero-Sanchez B, Addo P, Buyukaksoy A, Birss V. Performance enhancement of La0.3Ca0.7Fe0.7Cr0.3O3-δ air electrodes by infiltration methods. J Electrochem Soc. 2017;164(10):F3123–30.

How to cite this article: Akkurt S, Sındıraç C, Egesoy TÖ, Atıcı G, Erişman E, Erğen E, et al. Effects of electrospraying parameters on deposition of $La_{0.3}Sr_{0.7}Fe_{0.7}Cr_{0.3}O_{3-\delta}$ cathode layer on GDC. Int J Appl Ceram Technol. 2022;1–14. https://doi.org/10.1111/ijac.14303